

Aerothermodynamic Testing of Protuberances and Penetrations on the NASA Crew Exploration Vehicle Heat Shield

Derek S. Liechty¹

NASA Langley Research Center, Hampton, VA, 23681-2199

An experimental wind tunnel program is being conducted in support of an Agency wide effort to develop a replacement for the Space Shuttle and to support the NASA's long-term objective of returning to the moon and then on to Mars. This paper documents experimental measurements made on several scaled ceramic heat transfer models of the proposed Crew Exploration Vehicle. Global heat transfer images and heat transfer distributions obtained using phosphor thermography were used to infer interference heating on the Crew Exploration Vehicle Cycle 1 heat shield from local protuberances and penetrations for both laminar and turbulent heating conditions. Test parametrics included free stream Reynolds numbers of $1.0 \times 10^6/\text{ft}$ to $7.25 \times 10^6/\text{ft}$ in Mach 6 air at a fixed angle-of-attack. Single arrays of discrete boundary layer trips were used to trip the boundary layer approaching the protuberances/penetrations to a turbulent state. Also, the effects of three compression pad diameters, two radial locations of compression pad/tension tie location, compression pad geometry, and rotational position of compression pad/tension tie were examined. The experimental data highlighted in this paper are to be used to validate CFD tools that will be used to generate the flight aerothermodynamic database. Heat transfer measurements will also assist in the determination of the most appropriate engineering methods that will be used to assess local flight environments associated with protuberances/penetrations of the CEV thermal protection system.

Nomenclature

d	=	compression pad/tension tie diameter (in)
D_1	=	model/vehicle maximum diameter (in)
D_2	=	model/vehicle base diameter (in)
h	=	heat transfer coefficient, $h = q/(H_{aw}-H_w)$, (lbm/ft ² /s)
H	=	enthalpy (btu/lbm)
k	=	discrete trip height (in)
L	=	model/vehicle length (in)
M	=	Mach number
p	=	pressure (psi)
r	=	radial location (in)
r_1	=	inner radial location ($r/R = 65\%$) for compression pad/tension tie parametrics (in)
r_2	=	outer radial location ($r/R = 85\%$) for compression pad/tension tie parametrics (in)
r_s	=	model/vehicle shoulder radius (in)
r_{bs}	=	model/vehicle base shoulder radius (in)
R	=	model/vehicle radius (in)
R_n	=	model/vehicle forebody heat shield radius (in)
T	=	temperature (°R)
q	=	surface heat transfer rate (btu/ft ² /s)
α	=	angle-of-attack (deg)
δ	=	boundary layer height (in)
ϕ	=	model orientation (rotation) angle (deg)

¹ Aerospace Engineer, Aerothermodynamics Branch, MS 408A, Member AIAA.

ψ = model/vehicle cone angle (deg)

Subscripts

∞ = free stream static conditions
 aw = adiabatic wall conditions
 FR = conditions from Fay-Riddell calculation for a hemisphere
 fs = full scale dimensions
 t, l = reservoir conditions
 w = wall conditions

I. Introduction

Officially designated as “Orion,” the Crew Exploration Vehicle (CEV) capsule will ultimately be capable of transporting four crewmembers for lunar missions and later supporting crew transfers for Mars missions. In the near term, Orion will be capable of transporting up to six crewmembers to and from the International Space Station. While similar to Apollo in many aspects, Orion must be cost effective and certain elements of the spacecraft reusable. To accommodate a larger crew compliment, the capsule will be much larger, with a heat shield diameter approximately 28.6% larger than Apollo (18.04 ft for Cycle 1 CEV vs. 12.83 ft for Apollo). The heat shield design (as of the tunnel entry date) uses a Phenolic Impregnated Carbon Ablator (PICA) to protect the spacecraft from heating during reentry into Earth’s atmosphere. Like Apollo, the CEV capsule and associated heat shield will remain attached to the service module until the end of a mission. The current plan for Orion’s return to Earth and landing includes a primary water-based touchdown, with a land-based touchdown as a back-up option.

An experimental heat transfer test has been performed at the NASA Langley Research Center (LaRC) on scaled 3.23% models of the Crew Exploration Vehicle (CEV) Cycle 1 Outer Mold Line (OML) configuration in order to determine interference heating patterns in the vicinity of protuberances and penetrations into the forebody heat shield. These local perturbations to the baseline smooth CEV OML were intended to be generic representations of proposed hardware designed to act as load paths and prevent torsional rotation of the Crew Module (CM) as it sits on the Service Module (SM) (see Figs. 1 and 2). The attachment hardware modeled in this wind tunnel test included both tension ties and compression pads, similar to the hardware found on Apollo^{1,2}. The attach hardware proposed for CEV, prior to the prime contractor down-select, called for eight equally-spaced compression pad/tension tie combinations near the heat shield shoulder. This test was conducted in the LaRC 20-Inch Mach 6 Air Tunnel for a free stream Reynolds number range from $1.0 \times 10^6/\text{ft}$ to $7.25 \times 10^6/\text{ft}$, and a nominal re-entry angle-of-attack of 152 degrees (see Fig. 3 for definition of angle of attack). The effects of the state of the approaching boundary layer (laminar/turbulent) were also investigated. Compression pad diameter, radial and angular location, and



Figure 1. Orion Crew Module and Service Module.

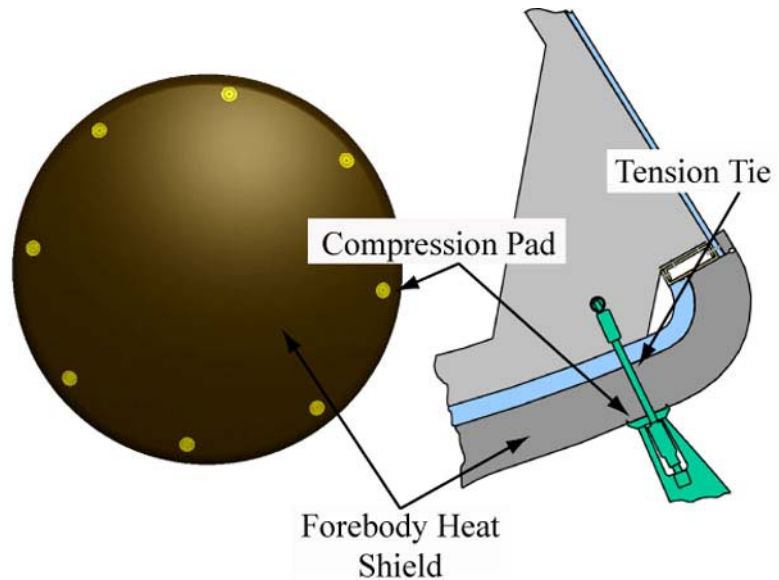


Figure 2. Compression pad layout on forebody heat shield and compression pad/tension tie schematic when CM and SM are joined.

Table 1. Nominal and measured flow conditions for the current test in the 20-Inch Mach 6 Air Tunnel.

$Re_{\infty, \text{nominal}}/\text{ft} \times 10^6$	$Re_{\infty}/\text{ft} \times 10^6$	M_{∞}	$P_{t,1}$	$T_{t,1}$
1	1.08±0.007	5.89±0.018	60.48±1.29	875.25±2.97
2	2.08±0.004	5.96±0.028	125.15±1.66	902.59±3.83
3	2.95±0.001	5.99±0.045	180.61±3.07	905.84±3.96
4	4.08±0.004	6.01±0.072	251.53±3.76	906.48±4.48
5	5.05±0.001	6.03±0.056	326.36±2.87	932.37±5.34
5.7	5.67±0.004	6.03±0.070	367.18±3.57	932.61±4.60

geometry were also parameters tested. The tension tie location was also varied between being concentric with the compression pad and outboard of the compression pad.

II. Experimental Methods

A. Test Facility

The test was conducted in the 20-Inch Mach 6 Air Tunnel, a facility in the Langley Aerothermodynamics Laboratory (LAL) at NASA LaRC. More detailed information on this tunnel and other LAL facilities can be found in References 3 and 4. The 20-Inch Mach 6 Air Tunnel is a blow down wind tunnel that uses heated, dried and filtered air as the test gas. The tunnel has a two-dimensional, contoured nozzle, which opens into a 20.5-in by 20-in test section. Models are mounted on a hydraulic injection system located in a housing below the closed test section that can deliver the model to the tunnel centerline in less than 0.5 second. Run times of up to 15 minutes are possible in this facility, although for the current aeroheating study, run times of only a few seconds were required. The nominal reservoir conditions of this facility are stagnation pressures of 30 psi to 500 psi with stagnation temperatures of 300 °F to 540 °F, in which the free stream and post-shock flow behaves as a perfect gas ($\gamma \approx 1.4$) with Mach numbers between 5.8 and 6.1 and Reynolds numbers of $0.5 \times 10^6/\text{ft}$ to $7.3 \times 10^6/\text{ft}$. Nominal test conditions for the 20-Inch Mach 6 Air Tunnel are presented in Table 1 along with the run-to-run repeatability for the current test.

B. Global Surface Heating Technique

A two-color, relative-intensity phosphor thermography technique⁵⁻⁸ was used to obtain global experimental aeroheating data in the wind tunnel. This technique uses a mixture of phosphors that, when illuminated with ultraviolet light, fluoresce in the bands of the visible spectrum, of which the red and green bands are used. The intensity of the fluorescence is dependent upon the amount of incident ultraviolet light and the local surface temperature of the phosphor. This phosphor mixture, which is suspended in a silica ceramic binder and applied with an airbrush, is used to coat the slip cast silica ceramic models. The final coating thickness is approximately 0.001 in. Using a 3-CCD (Charge Coupled Device) camera, fluorescence intensity images of an illuminated phosphor model exposed to the tunnel flow are acquired and converted to temperature mappings via a temperature-intensity calibration. The temperature calibration uses the ratio of the red and green components of the image to construct a lookup table, which converts the relative intensities to temperature values. Currently, this calibration, done prior to the test, is valid over a temperature range from 532 °R to 800 °R. The temperature data from the time-sequenced images taken during the wind tunnel run are then reduced to enthalpy based heat transfer coefficients at every pixel of the image (and hence globally on the model) using a heat-transfer rate calculation assuming one-dimensional semi-infinite slab heat conduction⁵. The model was mounted such that the surface to be measured was visible through the tunnel-ceiling window. The camera was aligned approximately perpendicular to the model surface being viewed (see Fig. 3).

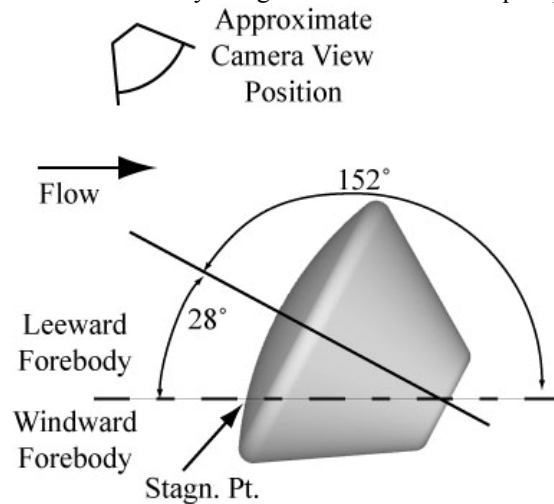


Figure 3. Model setup in wind tunnel.

Table 2. Nominal and measured dimensions (see Fig. 4 for nomenclature).

Model Designation	D_1 (in)	D_2 (in)	R_n (in)	r_s (in)	r_{bs} (in)	L (in)	ψ (deg)
Model Nominal	7.0000	2.5281	8.4000	0.3500	0.3500	4.6035	32.5000
Cycle 1 OML	216.54	78.20	259.84	10.83	10.83	142.40	32.50
Cycle 2 OML	198.00	71.79	237.60	9.90	2.00	130.00	32.50
CEV-PEN-1	6.9480	2.4910	8.3900	0.3178	0.3683	4.5926	32.3713
CEV-PEN-2	6.9529	2.4848	8.2447	0.3306	0.3492	4.6020	32.4153
CEV-PEN-3	6.8924	2.5667	8.4531	0.3077	0.2879	4.5874	32.5279
CEV-PEN-4-1	6.9352	2.7225	8.3749	0.3155	0.2973	4.5815	32.4729
CEV-PEN-4-2	6.8919	2.7392	8.6573	0.3067	0.3028	4.5642	32.2783
CEV-PEN-5	6.9480	2.4865	8.4062	0.3131	0.3597	4.5909	32.3612
CEV-PEN-6	6.9364	2.6373	8.2571	0.3712	0.3033	4.5895	32.4639

C. Test Model Description

The Cycle 1 OML of the CEV command module is a blunt body capsule with a diameter of 18.04 ft, resulting in a 7-in. diameter model at 3.23% scale. However, since the OML had been changed immediately prior to the tunnel entry to the Cycle 2 OML, the compression pads and tension ties needed to be scaled to the new flight geometry. The Cycle 2 OML of the CEV command module is also a blunt body capsule now with a diameter of 16.5 ft, resulting in a 7-in diameter model at 3.5% scale. A reference OML can be seen in Fig. 4 with dimensions listed in Table 2. Table 2 includes the nominal model dimensions, Cycles 1 and 2 full-scale dimensions, and the measured dimensions of the seven models tested (six configurations with one backup model).

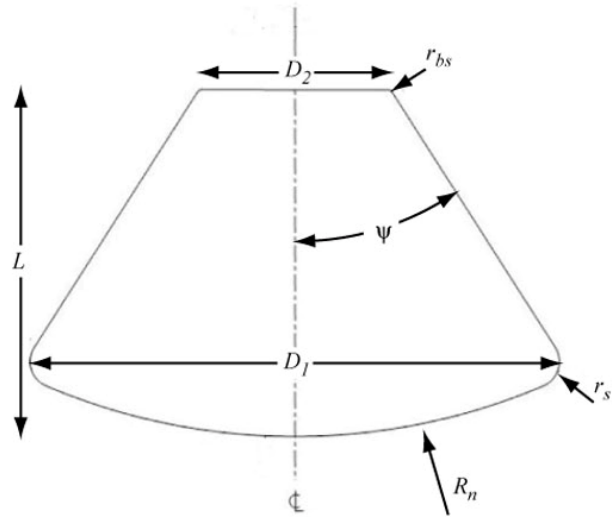


Figure 4. Geometric parameters of the CEV crew module.

The 7-in cast ceramic models used in the present test series were manufactured from molds created from rapid prototype resin patterns. Standard methods, materials, and equipment developed at the NASA LaRC were used in fabricating the ceramic aeroheating test models⁹. Due to the symmetry of the CEV capsule models, casting molds were created directly from the resin patterns, bypassing the wax pattern requirement. It is note worthy, as in general it has been determined that wax patterns introduce the largest uncertainty in the final ceramic OML due to wax shrinkage. All models were supported by a 1-in diameter cylindrical, stainless steel sting aligned concentric to the model axis of symmetry. The ratio of base diameter to sting diameter was 2.53.

Fiducial marks were applied to the model surface using a coordinate measuring machine. The reference marks on the model surface were used to align the model in the tunnel, determine the attachment hardware locations and to aid in any future applications involving mapping of the 2-D image data to a 3-D CAD wire frame geometry.

Several attachment hardware concepts were being evaluated at the time this study was performed. The configurations that were investigated in this study are shown in Fig. 5. The first was an annular trench with the center of the compression pad flush with the surrounding heat shield. The second configuration was a circular penetration with the floor of the compression pad recessed below the surrounding heat shield. The penetration sizes were scaled from the full-scale compression pad diameter (estimated to be 6-in at the time of the test) by multiplying the full-scale diameter by the ratio of the average model boundary layer thickness to the average full-scale vehicle boundary layer thickness. This scaling was done by using the code LAURA¹⁰ to calculate flight (peak convective heating) and wind tunnel ($Re_\infty = 4.0 \times 10^6/\text{ft}$ and $8.0 \times 10^6/\text{ft}$) conditions, resulting in a

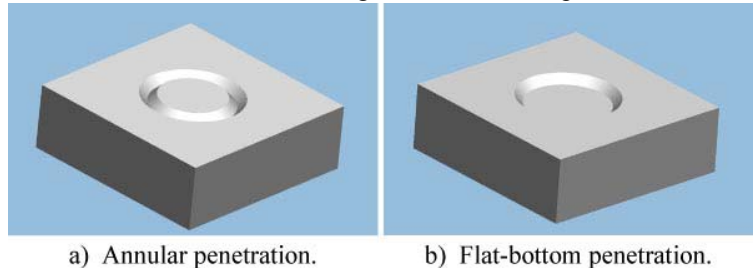


Figure 5. CEV compression pad configurations.

compression pad size that is slightly smaller than a direct geometric scaling (0.18-in compared to 0.21-in). As a secondary parameter, several other compression pad diameters were examined. These were 4- and 8-in full-scale diameter compression pads. All compression pads were added to the ceramic models by way of a laser ablation system, similar to the method used in the Shuttle Return to Flight study conducted at the LAL¹¹.

The current design of the CEV, like the Apollo capsule, not only has compression pad penetrations in the heat shield, but also has protrusions resulting from the tension ties. The estimations of tension tie diameter as of the time of the test ranged from about 0.5-in to 0.8-in. Small ceramic tubes with a diameter of 1/32-in. were used to simulate these tension ties. This diameter of tension tie results in a full-scale diameter of about 1-in. The ceramic tubes were applied to the model by drilling a hole slightly wider than the tube, and then a high temperature adhesive was used to fix the tube in the hole. The tube protruded above the surrounding model surface by about 0.18-in (6-in when scaled to the boundary layer height in flight). Two locations of the tube relative to the compression pads were considered. The first location resembled that of the Apollo capsule in that it is just outboard of the compression pad. The second configuration was a new location that was being considered and was concentric to the compression pad. The nomenclature used for all compression pad/tension tie configurations along with their representations in any schematics included in this report and a photograph of the configuration can be seen in Table 3.

A representative schematic of a model configuration is presented in Fig. 6. The compression pad numbering scheme is presented in this figure. Pads 1 through 4 are annular pads while numbers 5 through 8 are recessed pads. To test another parametric on each model, pads 1, 2, 5 and 6 are at the outer radial location, while pads 3, 4, 7 and 8 are at the inner radial location. An angle ϕ is discussed in this report and refers to the model orientation. In Fig. 6, the model is in the $\phi = 0$ -deg. orientation. When the model is in the $\phi = 180$ -deg. orientation, it is simply rotated 180-deg. about the model axis. While the pad numbers rotate with the model, the letter assigned to each angular location (A-H) remains constant. In other words, if pad location A is referenced, it is referring to the compression pad located 22.5 degrees clockwise from the leeward centerline of the model. For CEV-PEN-2, this could be pad number 3 (annular, $\phi = 0$ -deg) or pad number 7 (recessed, $\phi = 180$ -deg). The rationale behind the model design in terms of compression pad parametric layout derives from the fact that if the model is tested at both $\phi = 0$ - and 180-deg, each parametric has been tested at the equivalent of each of the 8 compression pad locations on the vehicle since the vehicle is symmetric about the vertical plane.

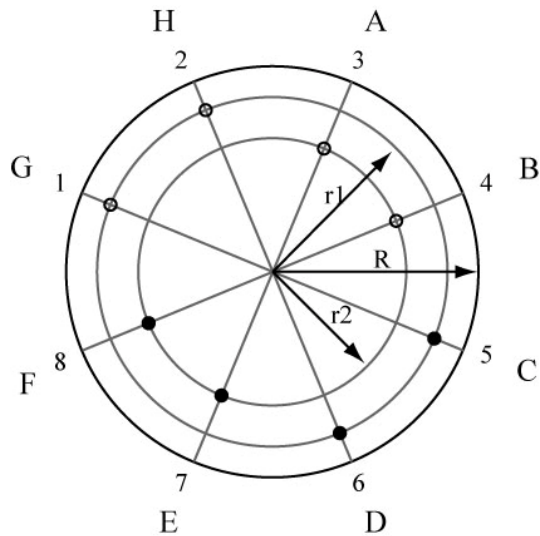


Figure 6. Representative schematic of compression pad/tension tie model configurations (open circle annular pad; closed circle recessed pad)

Table 3. CEV compression pad/tension tie configurations with schematics and images.

Configuration	Schematic Image	Model Photo
Baseline	N/A	N/A
Annular Compression Pad No Tension Tie		
Recessed Compression Pad No Tension Tie		
Annular Compression Pad Outboard Tension Tie		
Recessed Compression Pad Outboard Tension Tie		
Annular Compression Pad Concentric Tension Tie		
Recessed Compression Pad Concentric Tension Tie		

Two locations of the tube relative to the compression pads were considered. The first location resembled that of the Apollo capsule in that it is just outboard of the compression pad. The second configuration was a new location that was being considered and was concentric to the compression pad. The nomenclature used for all compression pad/tension tie configurations along with their representations in any schematics included in this report and a photograph of the configuration can be seen in Table 3.

A list of model configurations used in this study (total of 6) along with a brief description can be viewed in Table 4. Model CEV-PEN-1 was a baseline model with no penetrations or protuberances on the model. This serves as a reference as to how the compression pads and tension ties affect surface heating. Model CEV-PEN-2 (shown in Fig. 6) contains only compression

Table 4. Model designations and descriptions.

Model Designation	Description
CEV-PEN-1	Baseline configuration, no compression pads or tension ties
CEV-PEN-2	Annular and recessed compression pads, $D_{fs} = 6\text{-in}$, $r/R = 0.65, 0.85$
CEV-PEN-3	Same as CEV-PEN-2 with tension ties downstream of compression pads
CEV-PEN-4	Same as CEV-PEN-2 with tension ties concentric with compression pads
CEV-PEN-5	Annular compression pads, $D_{fs} = 4\text{-in}, 8\text{-in}$, $r/R = 0.65, 0.85$
CEV-PEN-6	Recessed compression pads, $D_{fs} = 4\text{-in}, 8\text{-in}$, $r/R = 0.65, 0.85$

pads (6-in full scale diameter). The model was split into four quadrants. Two of the four contain the annular compression pad; the other two quadrants contained the recessed compression pad. For each type of compression pad, two radial locations were examined, one being at 85% of the model radius, the other located at 65% of the model radius. This penetration arrangement was used for the remaining four model configurations. Model CEV-PEN-3 was identical to CEV-PEN-2 except it included the outboard tension tie. Model CEV-PEN-4 was similar to CEV-PEN-2 except that it included the concentric tension tie. Model CEV-PEN-5 varied the size of the annular compression pad (4-in and 8-in full scale diameters) at the two radial locations, whereas model CEV-PEN-6 varied the size of the recessed compression pad. Please see Ref. 12 for all compression pad and tension tie dimensions.

D. Data Reduction and Uncertainty

Flow condition data was acquired using a 16-bit analog-to-digital facility acquisition system. The values of $p_{t,i}$ and $T_{t,i}$ are accurate to within $\pm 2\%$. The uncertainties in the angle-of-attack of the model are $\pm 0.2\%$.

A one-dimensional, semi-infinite solid heat-conduction equation is used to calculate the heating rates from the global surface temperature measurements⁵. The estimated experimental uncertainty of the heating results as obtained by the thermographic phosphor system is a function of fluorescent intensity, which is dependent on model surface temperature. For higher surface temperatures (greater than 720 °R), such as those on most of the forebody heat shield, the uncertainty⁵ is approximately $\pm 8\%$ to $\pm 10\%$, while for lower temperatures (less than 585 °R); the uncertainty is approximately $\pm 15\%$ to $\pm 20\%$. Additional measurement uncertainty can be introduced due to internal three-dimensional heat conduction in high-gradient regions such as compression pad corners. This uncertainty is estimated to vary from less than $\pm 5\%$ at the lowest Reynolds number to greater than $\pm 10\%$ at the highest Reynolds numbers (Reynolds number dependence due to the lower surface temperature rise at low Reynolds numbers).

Uncertainties can be introduced when extracting line cut data from an image due to perspective distortion of the image, lack of pixel resolution in high-gradient regions, and lack of precision in locating fiducial marks. These errors are estimated to be less than $\pm 5\%$ on relatively flat surfaces and up to $\pm 10\%$ on highly curved surfaces.

A square root of the sum-of-the-squares estimate for the total uncertainty based on the above factors gives a worst-case experimental uncertainty range of $\pm 13\%$ on flat areas of the forebody heat shield. In addition to the sources of experimental uncertainty discussed above, additional uncertainty in transition onset may also be influenced by inherent differences in model surface roughness between models or coating degradation which occurs over the length of a test due to handling of the model and pitting of the surface from particle impacts. Because this uncertainty increases over time and varies from model to model, no fixed value for the uncertainty is assigned. These uncertainties can be applied to global heating rates. Because of increased uncertainties in conduction errors and phosphor coating uniformity around the compression pads and tension ties, local heating rates immediately surrounding these OML features are qualitative results only.

E. Data Format

Global heating images and either representative centerline data cuts or data cuts downstream of compression pad/tension tie locations are provided in this paper. Centerline data for the CEV models are presented as normalized heating rates h/h_{FR} vs. the normalized radial location r/R . The reference heating value, h_{FR} , is based on the Fay-Riddell¹³ hemisphere stagnation point heating with a nose radius of 8.4-in and a wall temperature of 540 °R. Data cuts extending from just upstream of the compression pads extending downstream to the model shoulder, comparing Reynolds number and other parameters tested, are presented in the normalized heating rate h/h_{FR} vs. the pixel number from the point where the data cut started. This “distance” variable of pixels should not be correlated to any distance or radial location on the CEV model. In this study, the dimensional distance has not been quantified in terms of absolute position. Therefore, even though the heating rates downstream of the compression pad are qualitative, the distance variable is qualitative.

III. Experimental Results

A. Global Forebody Aeroheating

The following includes discussions of general trends observed from the global forebody aeroheating images. One important note to make when analyzing the data is the state of the approaching boundary layer. This mainly effects data on pad locations F and G. This is due to the placement of the compression pads on the model surface. These pad locations have other pads upstream that, if effective at tripping the boundary layer, have the potential to affect the downstream compression pad.

Centerline heating data is shown in Figure 7 as a function of Reynolds number along with a CFD prediction (from LAURA). Very good agreement is shown over most of the leeward surface of the model. The agreement begins to worsen towards the windward shoulder. This is mostly attributed to the fact that the camera was positioned such that the leeward surface of the forebody was more normal to the camera. This was not purposeful, but was a limit of the windows in the tunnel and model support hardware.

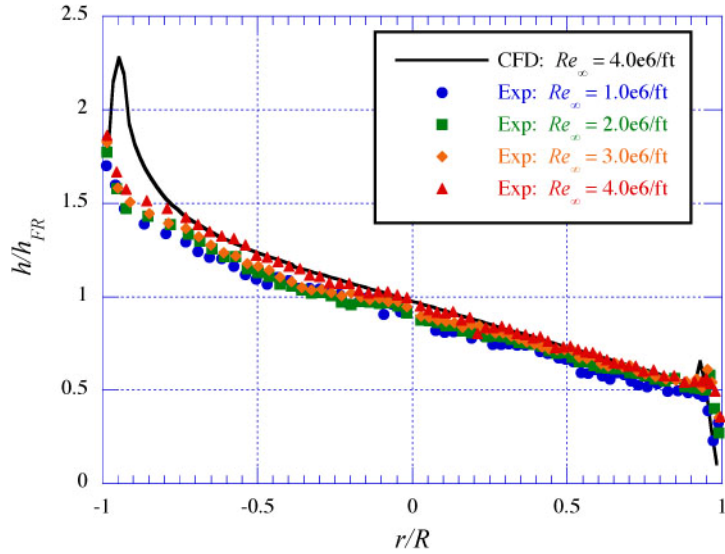


Figure 7. Representative schematic of compression pad/tension tie model configurations.

1. Effect of Reynolds Number

The influence of changing the free stream Reynolds number is exemplified in Fig. 8. The model shown is CEV-PEN-2 at $\phi = 0$ -deg (annular pads on top; recessed pads on bottom). The effectiveness of the compression pad at tripping the flow to transitional/turbulent increased as the free stream Reynolds number increased. This trend held true for all models regardless of the compression pad/tension tie configuration.

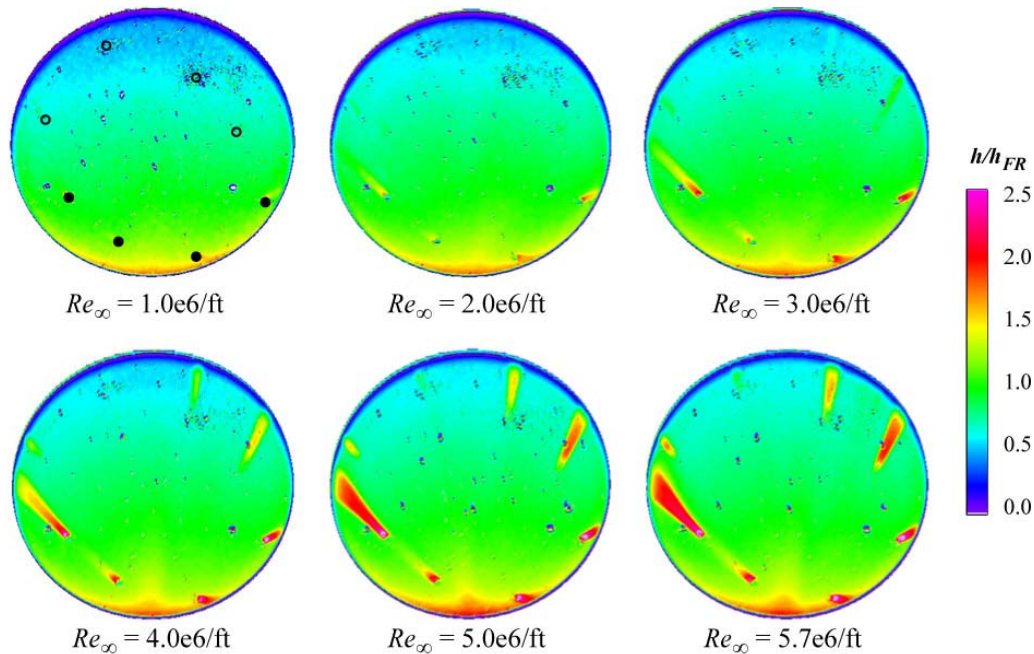


Figure 8. Effect of changing free stream Reynolds number for model CEV-PEN-2 at $\phi = 0$ -deg (pad locations shown in $Re_\infty = 1e6/ft$ image as open circles for annular and closed for recessed).

B. Compression Pad/Tension Tie Local and Downstream Aeroheating Results

One of the objectives of this study was to observe local, qualitative heating phenomena immediately surrounding the compression pad/tension tie locations as well as the downstream effects. To this end, a limited number of runs were made where the camera was optically zoomed on pad locations A and F. Figure 9 presents compression pad location A, $\phi = 180$ -deg (recessed pad) with an approaching laminar boundary layer (at $Re_\infty = 2.0 \times 10^6/\text{ft}$) and a tripped turbulent approaching boundary layer (at $Re_\infty = 5.0 \times 10^6/\text{ft}$) for models CEV-PEN-2, CEV-PEN-3, CEV-PEN-4 and CEV-PEN-6 (larger diameter pad). Turbulent heating could not be achieved “naturally,” so a boundary layer tripping strategy was developed based on a limited test entry into the 20-Inch Mach 6 Air Tunnel¹⁴ (see Fig. 11). Based upon this CEV trip screening study, trips for this study were placed in a location and pattern that would ensure uniform turbulent heating to the portion of the heat shield being focused on. The isolated roughness elements used in this study consisted of adhesively backed high temperature tape that was pre-cut with a laser to the desired square planform shape. Height parametrics were controlled by the tape thickness. The 0.05 x 0.05-in protuberances were placed as a single array located well upstream of the compression pad/tension tie of interest. A trip height of 0.0115-in was tested and corresponded to a k/δ of approximately 0.9 at a unit Reynolds number of $4.0 \times 10^6/\text{ft}$ (based on CFD results using LAURA).

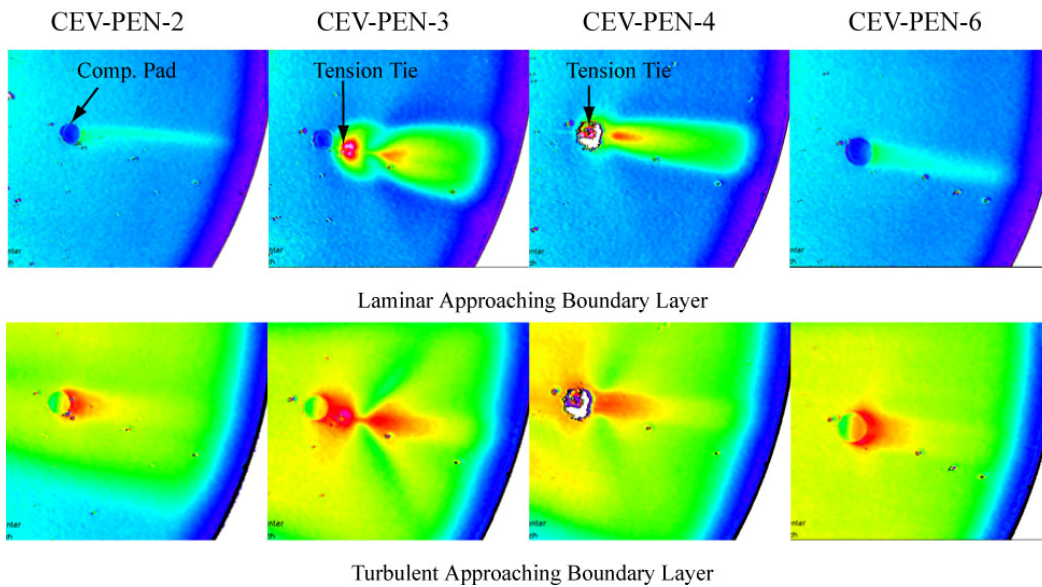


Figure 9. Zoomed view of pad location A.

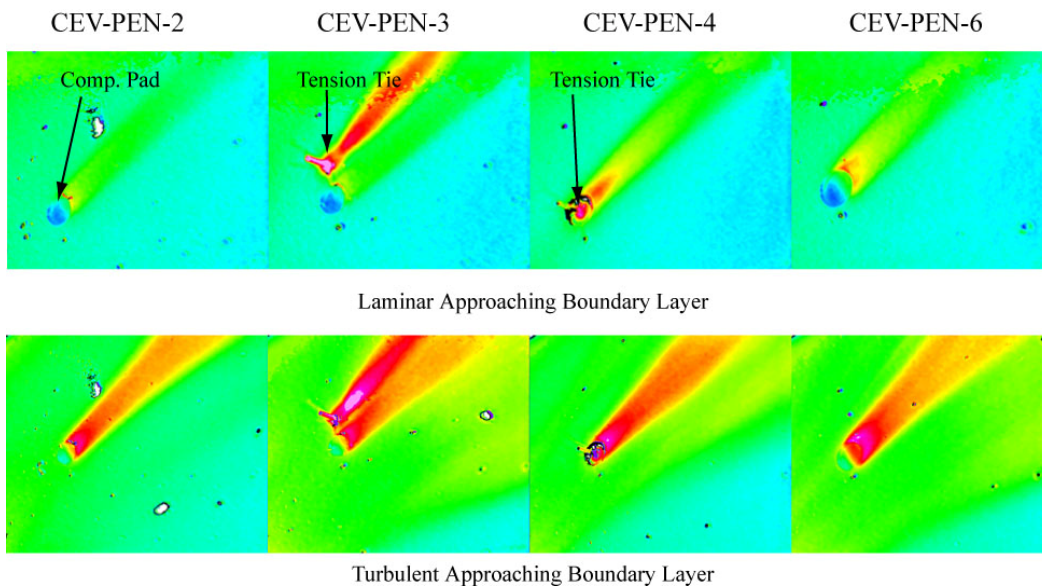


Figure 10. Zoomed view of pad location F.

In the following discussion, the line cuts in Figs. 12, 13 and 14 are taken from the global views (which are all laminar runs). Only Figs. 15 and 16 are taken from the above optically zoomed images.

1. Effect of Reynolds Number

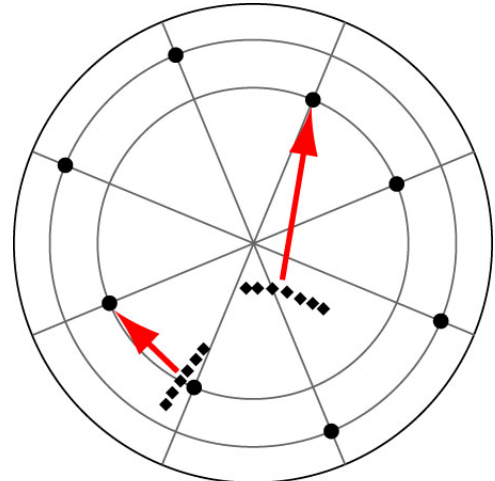
The influence of changing the free stream Reynolds number is exemplified in Fig. 12 for pad location B, both annular and recessed pad configurations (no tension tie present). As expected, the effectiveness of the compression pad at tripping the flow to transitional/turbulent increased as the free stream Reynolds number increased. This trend holds true regardless of the compression pad/tension tie configuration. For the recessed compression pad, the heating levels on the pad floor can be seen to increase as the Reynolds number is increased.

2. Effect of Compression Pad Configuration

The effect of varying compression pad configuration at a fixed pad location can be viewed in Fig. 12 for pad location B. In these plots, the annular is on the left, while the recessed pad is on the right. The recessed compression pad configuration was more effective at tripping the boundary layer to transitional/turbulent heating levels. This trend intuitively makes sense because the recessed compression pad is a greater perturbation to the original OML (more material was removed). The flow has a greater opportunity to turn into the compression pad.

3. Effect of Tension Tie Configuration

The effect of varying the tension tie configuration at a fixed pad location can be viewed in Fig. 13. The annular compression pad configuration is presented in this figure and the baseline (CEV-PEN-1) is compared to the pad-only (CEV-PEN-2), the outboard tie (CEV-PEN-3), and the concentric tie (CEV-PEN-4). These configurations can also be viewed in Fig. 9 as optically zoomed phosphor thermography images. In general, the outboard tension tie configuration resulted in slightly higher downstream heating levels as compared to the concentric tension tie configuration. The concentric tension tie configuration peaked before the outboard configuration, but the outboard configuration's peak was slightly higher for a given Reynolds number. Another point to consider is the fact that the concentric tension tie configuration causes much higher heating on the floor of the compression pad (see Fig. 10, CEV-PEN-3 vs. CEV-PEN-4). This could potentially have an important impact on the choice of thermal protection used for the compression pads.



Note: Discrete trip locations/orientations/sizes not exact.

Figure 11. Approximate discrete trip locations.

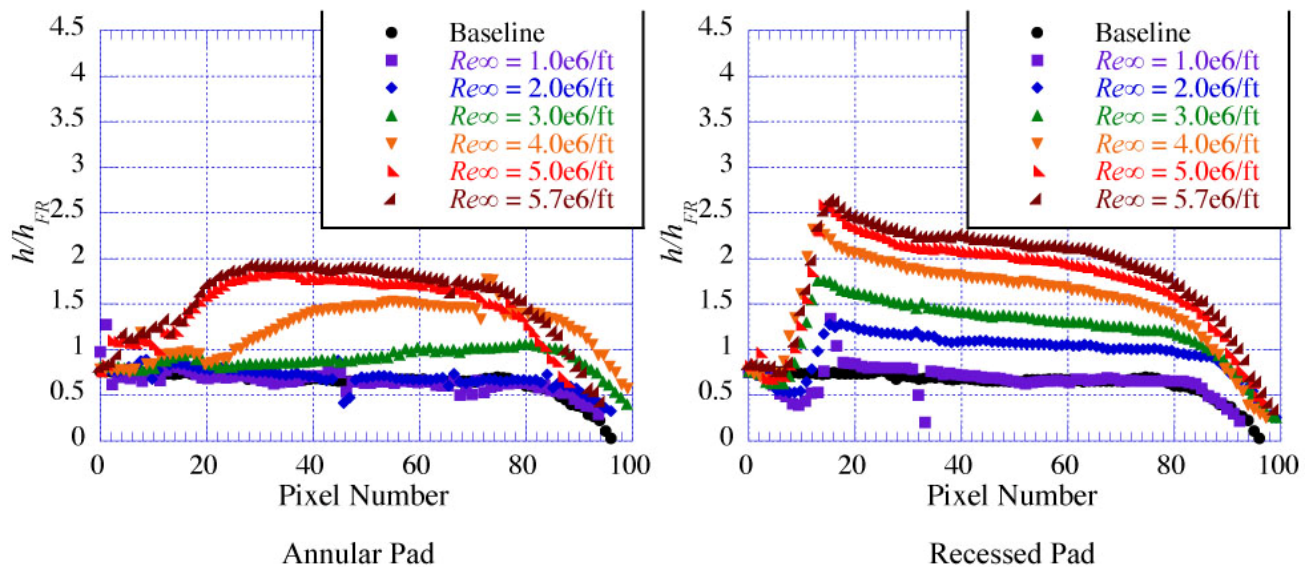


Figure 12. Effect of compression pad configuration as free stream Reynolds number changes at pad location B.

4. Effect of Compression Pad Size

The effect of varying compression pad size can be viewed in Fig. 14. As the diameter of the compression pad increased, so did its effectiveness at tripping the boundary layer to a transitional/turbulent state. As with the effect of compression pad configuration, this trend was expected since the perturbation to the OML increased as the size of the compression pad increased. This is mainly a local effect to the compression pad location; no real difference is observed downstream of the pad location. The 6-in and 8-in full scale diameter recessed compression pads can be viewed in Figs. 9 and 10 for pad locations A and F, respectively.

5. Effect of Approaching Boundary Layer

Data from the all of the optically zoomed images in Figs. 9 and 10 are presented as line cuts in Figs. 15 and 16, respectively. Most of the line cuts in these figures were taken from just upstream of the compression pad along the streamline to the shoulder, as described previously. For the outboard tension tie configuration from pad location F, one additional data cut was included since the streamline through the tension tie did not coincide with the streamline through the compression pad. This was done because the increase in heating levels caused by the tension tie was greater than that of the compression pad.

One interesting point to note are the differences in peak heating levels between the laminar and turbulent boundary layer cases. For the configurations that included the tension tie, the peak heating levels appeared to decrease with an approaching turbulent boundary layer. This is most probably due to the thinner boundary layer associated with the laminar cases where the energy outside of the boundary layer has less distance to penetrate to get to the surface of the vehicle once the tension tie disturbs the flow.

Another trend is the difference in heating levels after the compression pad locations between locations A and F over the baseline heating levels for the turbulent approaching boundary layer cases. For pad location A, the difference between the baseline case and the compression pad/tension tie configurations is much less than that for pad location F.

There is also a difference in heating level patterns on the floor of the recessed compression pad as the state of the approaching boundary layer changes. For the laminar approaching boundary layer (see Figs. 9 and 10), it doesn't appear that the flow turns into the compression pad (the heating levels remain relatively constant). For the turbulent approaching boundary layer, about half way across the compression pad, the heating levels increase, indicating the shear layer has impacted the compression pad floor.

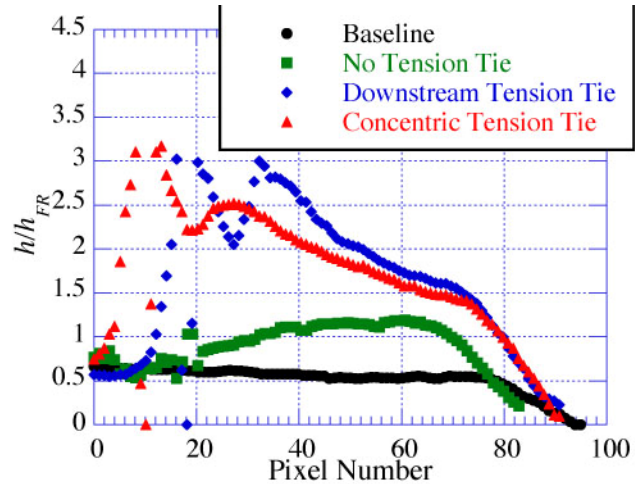


Figure 13. Effect of tension tie configuration at $Re_\infty = 4.0 \times 10^6/\text{ft}$, pad location A.

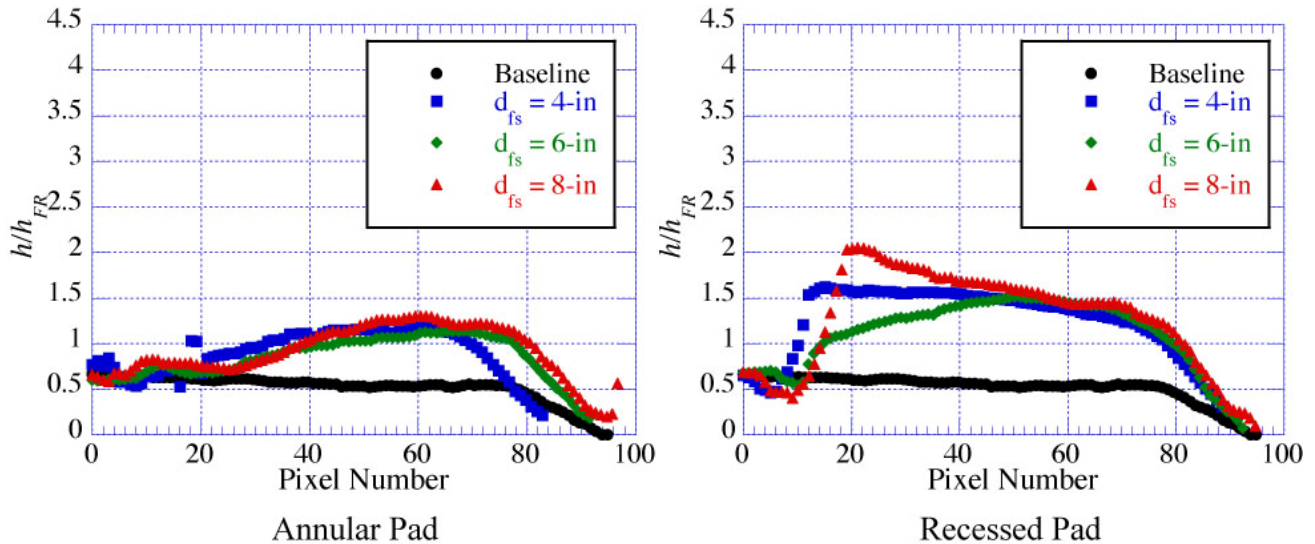


Figure 14. Effect of compression pad size for the annular and recessed pad configurations, pad location B.

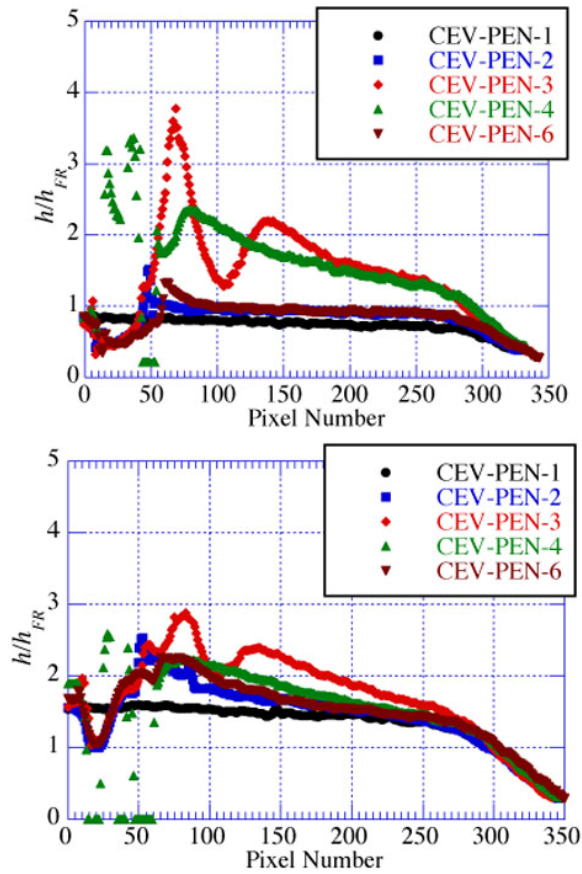


Figure 15. Data cuts from zoomed pad location A.

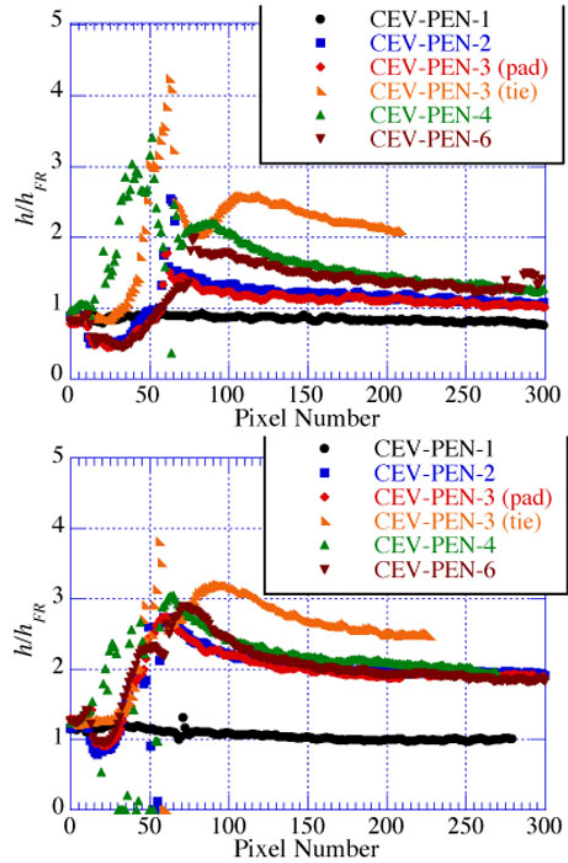


Figure 16. Data cuts from zoomed pad location F.

IV. Conclusion

An experimental heat transfer test has been performed in the NASA Langley Research Center 20-Inch Mach 6 Air Tunnel on scaled models of the Orion Crew Exploration Vehicle. Due to the need to keep the Crew Module attached to the Service Module, compression pads and tension ties are required and will result in surface perturbations in the forebody heat shield. The focus of the current study was to determine the interference patterns in the vicinity of these compression pads and tension ties over a range of free stream Reynolds numbers and compression pad/tension tie configurations.

The effects of approaching boundary layer state, Reynolds number, compression pad configuration, tension tie configuration, and compression pad size and location were investigated. In general, the effectiveness of any compression pad/tension tie configuration at tripping the boundary layer to transitional/turbulent increased as the free stream Reynolds number was increased. The recessed compression pad produced a much larger increase in heating levels as compared to the annular compression pad. The outboard tension tie configuration produced slightly higher heating levels than the concentric tension tie configuration. Another important observation pertaining to the tension tie location is its effect on the compression pad heating levels and the choice of thermal protection materials used for the compression pad. As the size of the compression pad increased, so did its effect on the state of the boundary layer.

When the approaching boundary layer was tripped to turbulent, it was found that, when the tension tie is included, the peak heating levels decreased as compared to a laminar approaching boundary layer. Also, if the approaching boundary layer is turbulent, the flow impinges on the floor of the recessed compression pad, while this did not occur with a laminar approaching boundary layer.

Acknowledgments

The author would like to acknowledge the contributions of the following individuals to this research: Harry Stotler, Grace Gleason, Rhonda Mills, Kevin Hollingsworth, and Teck-Seng Kwa for operation of the 20-Inch Mach 6 Air Tunnel and data acquisition support; Mark Griffith and Thomas Skalski for fabrication of the ceramic test models; John Hopkins for compression pad placement; Ronald Deans and Kathy Kuykendoll for model fidelity measurements and fiducial mark placement; John Dec, Randy Lillard and Benjamin Kirk for their inputs and suggestions; and Brian Hollis and Maria Pulsonetti for LAURA computations.

References

- ¹Jones, R. A., "Experimental Investigations of the Overall Pressure Distribution, Flow Field, and Afterbody Heat-Transfer Distribution of an Apollo Reentry Configuration at a Mach Number of 8," NASA TM X-813, June 1963.
- ²Bertin, J. J., "The Effect of Protuberances, Cavities, and Angle of Attack on the Wind-Tunnel Pressure and Heat-Transfer Distribution for the Apollo Command Module," NASA TM X-1243, October 1966.
- ³Miller, C. G., "Langley Hypersonic Aerodynamic/Aerothermodynamic Testing Capabilities – Present and Future," AIAA 90-1376, June 1990.
- ⁴Micor, J. R., "Langley Aerothermodynamics Facilities Complex: Enhancements and Testing Capabilities," AIAA 98-0147.
- ⁵Merski, N. R., "An Improved Two-Color Relative-Intensity Phosphor Thermography Method For Hypersonic Wind Tunnel Aeroheating Measurements," NASA CDTP-1017, February 2001.
- ⁶Merski, N. R., "Global Aeroheating Wind-Tunnel Measurements Using Improved Two-Color Phosphor Thermography Model," *Journal of Spacecraft and Rockets*, Vol. 36, No. 2, 1998, pp. 160-170.
- ⁷Buck, G. M. "Automated Thermal Mapping Techniques Using Chromatic Image Analysis," NASA TM 101554, April 1989.
- ⁸Merski, N. R., "Reduction and Analysis of Phosphor Thermography Data with IHEAT Software Package," AIAA 98-0712.
- ⁹Buck, G. M. and Vasques, P., "An Investment Ceramic Slip-Casting Technique for Net-Form Precision, Detailed Casting of Ceramic Models," U.S. Patent 5,266,252, November 30, 1993.
- ¹⁰Cheatwood, F. M. and Gnoffo, P. A., "User's Manual for the Langley Aerothermodynamic Upwind Relaxation Algorithm (LAURA)," NASA TM 4674, 1996.
- ¹¹Buck, G. M., "Fabrication of 0.0075-Scale Orbiter Phosphor Thermography Test Models for Shuttle RTF Aeroheating Studies," NASA TM 2006-214303, 2006.
- ¹²Liechty, D. S., "Aerothermodynamic Testing of Protuberances and Penetrations on the NASA Cycle I Crew Exploration Vehicle Heat Shield in the NASA Langley 20-Inch Mach 6 Air Tunnel: Test 6918," NASA EG-CAP-06-155, November 2006.
- ¹³Fay, J. A. and Ridell, F. R., "Theory of Stagnation Point Heat Transfer in Dissociated Air," *Journal of Aeronautical Sciences*, Vol. 25, No. 2, 1958, pp. 73-85.
- ¹⁴Berger, K. T., "Aerothermodynamic Testing of the Crew Exploration Vehicle in the LaRC 20-Inch Mach 6 and 31-Inch Mach 10 Tunnels," AIAA 2008-1225, January 2008.